Lab on a Chip

PAPER

Published on 08 September 2026
Licensed under CC-BY 4.0

Check for updates

Cite this: *Lab Chip*, 2026, **26**, 5962

Soft X-ray transparent flow cell for water window microscopy with integrated dielectrophoretic cell handling

Simone de Carli,†[ab] Julius Reinhard,†[cd] Sophia Kaleta,†[cd] Wilhelm Eschen,[de] Chang Liu,[de] Christian Guernth-Marschner,[a] Marine Vallet,[fg] Julie A. Z. Zedler,[h] Leona Licht,[de] Gerhard G. Paulus,[cd] Silvio Fuchs,[cdi] Neus Godino,*[a] Jan Rothhardt[dej] and Michael Kirschbaum*[a]

Soft X-ray (SXR) microscopy in the water window (284–543 eV) is a powerful technique enabling label-free whole-cell imaging with an intrinsic structural contrast. Studying living cells in their native aqueous environment, rather than cryopreserved specimens, allows direct, time-resolved observation of biological processes and yields physiologically relevant insights. However, imaging hydrated biological specimens under the vacuum conditions required for SXR microscopy remains challenging, requiring sample environments that simultaneously provide liquid confinement, vacuum compatibility, stable cell positioning, and efficient sample handling. Existing SXR-transparent flow cells often rely on artificial adhesion or fixation, limiting active manipulation and efficient turnover. Here, we present a vacuum-compatible microfluidic flow cell for water-window SXR microscopy with integrated dielectrophoretic (DEP) cell and particle handling. The device combines X-ray-transparent silicon nitride (Si_3N_4) membranes, microfluidic sample exchange, and DEP-based trapping of suspended cells within a thin liquid layer. Unlike conventional static sample holders, the platform allows fluidic replacement of samples without venting the microscope and enables controlled handling of individual suspended cells in their native aqueous environment. Using polystyrene particles and Jurkat cells, we characterized the DEP trapping performance and demonstrate stable confinement within the microfluidic channel. Integrated with a laboratory-based water-window SXR microscope, the platform enables imaging of dielectrophoretically trapped algal cells from different species in liquid during a single days-long vacuum session. These results establish the feasibility of combining DEP-based cell handling, microfluidic sample exchange, and water-window SXR microscopy in a single experimental platform and provide a foundation for future studies requiring controlled manipulation of hydrated cells during SXR imaging.

Received 1st April 2026,
Accepted 31st August 2026

DOI: 10.1039/d6lc00276e

rsc.li/loc

Introduction

The understanding of cellular biology is closely linked to the ability to observe cellular structures with ever-increasing detail.[1] Since the earliest observations, microscopy has been an essential tool for advancing biology, providing fundamental insights into cellular structures and mechanisms. Over the past decades, the development of high-resolution imaging techniques has provided crucial information on cellular morphology, essential for precisely distinguishing physiological from pathological processes.[2–7] This continuous evolution remains key not only to deepening

[a] *Fraunhofer Institute for Cell Therapy and Immunology, Branch Bioanalytics and Bioprocesses IZI-BB, Am Muehlenberg 13, 14476 Potsdam, Germany. E-mail: nieves.godino-amado@izi-bb.fraunhofer.de, michael.kirschbaum@izi-bb.fraunhofer.de*
[b] *Institute of Biotechnology, Technische Universität Berlin, Straße des 17. Juni, 135 10623 Berlin, Germany*
[c] *Institute of Optics and Quantum Electronics, Friedrich Schiller University Jena, Max-Wien-Platz, 107743 Jena, Germany*
[d] *Helmholtz-Institute Jena, Fröbelstieg 3, 07743, Jena, Germany*
[e] *Institute of Applied Physics, Abbe Center of Photonics, Friedrich-Schiller-Universität Jena, Albert-Einstein-Str. 15, 07745, Jena, Germany*
[f] *Institute for Inorganic and Analytical Chemistry, Friedrich Schiller University Jena, 07743 Jena, Germany*
[g] *Max Planck Fellow Group Plankton Community Interaction, Max Planck Institute for Chemical Ecology, 07745 Jena, Germany*
[h] *Matthias Schleiden Institute for Genetics, Bioinformatics and Molecular Botany, Friedrich Schiller University Jena, Philosophenweg 12, 07743 Jena, Germany*
[i] *Laserinstitut Hochschule Mittweida, University of Applied Science Mittweida, Technikumplatz 17, 09648 Mittweida, Germany*
[j] *Fraunhofer Institute for Applied Optics and Precision Engineering IOF, Albert-Einstein-Str. 7, 07745, Jena, Germany*
† These authors contributed equally to this work.

This journal is © The Royal Society of Chemistry 2026

our understanding of the intrinsic relationship between morphology and cellular function but also to guiding the development of targeted diagnostic and therapeutic strategies.[8–10]

In recent decades, research has shifted from the study of heterogeneous cell populations to the characterization of single cells, revealing a previously unrecognized functional and structural heterogeneity within the same tissue.[11–17] The need to further study the intrinsic biophysical properties of individual cells at higher resolutions has driven the development of imaging techniques capable of overcoming the limitations of traditional microscopy.[18–23] In this regard, SXR microscopy is emerging as an increasingly powerful imaging technique in biology.[24–26] By complementing existing methodologies, it bridges the gap between traditional imaging techniques and novel high-resolution approaches, offering the opportunity to study whole cells at the nanometric scale.[27–31] In this context, the so-called water window (284–543 eV) deserves particular attention. This energy range is perfectly suited for biological imaging, as carbon and nitrogen strongly absorb the radiation, while water remains relatively transparent, with a penetration depth of up to 23 μm (ref. 32) (T = 10%). The difference in absorption coefficients enables high-contrast imaging of biological specimens in their fully hydrated, native state without requiring staining or labelling.[32,33]

For these reasons, SXR microscopy currently offers a valuable opportunity to advance studies of subcellular structures with nanometric resolution, while preserving the native morphology of the specimens almost entirely. In particular, laboratory-based SXR microscopes based on laser-plasma sources[34–37] provide comparatively easy and flexible access to water-window imaging in a standard laboratory environment, enabling routine measurements and method development without the logistical constraints of large-scale synchrotron radiation facilities.

Because soft X-rays are strongly absorbed by air, these microscopes must operate under high-vacuum conditions, making cryo-fixation the standard sample-preparation approach, which additionally serves to minimize the impact of radiation damage.[31,34] While effective, this strategy imposes severe limitations, as it is technically demanding, limits investigations to single, isolated cells, and prevents imaging of living or freely suspended cells and sequential imaging of the same trapped cell before and after defined perturbations, *i.e.*, observing slowly evolving biological processes. Overcoming these constraints requires microfluidic systems capable of isolating and maintaining an aqueous environment within vacuum-compatible setups.

Previous approaches to liquid-phase SXR imaging have mainly relied on static Si_3N_4 sandwich cells without active flow[35–40] or on adhesion/fixation of cells to channel walls.[42] Consequently, true SXR-transparent flow cells have not been widely established, and existing approaches suffer from significant limitations: they do not support trapping suspended objects, restrict free spatial arrangement, complicate tomographic acquisition, and make sample replacement slow and laborious. Because replacing a sample often requires fabrication of an entirely new cell, the number of cells that can be investigated is severely limited.

In parallel, we and others have developed and employed octupole dielectrophoretic (DEP) field cages for highly stable trapping and 3D positioning of single particles and cells under ambient conditions.[41–44]

In this work, we combine these strands by redesigning the DEP cage on SXR-transparent Si_3N_4 membranes and integrating it into a vacuum-compatible flow cell. This device overcomes the previously mentioned limitations regarding adhesion-based sample handling (fixation, free spatial arrangement and consecutive sample analysis) by enabling non-invasive trapping of individual suspended cells and micro-objects in an aqueous environment, while simultaneously maintaining vacuum compatibility and soft X-ray transparency of the device. To our knowledge, this represents the first DEP-based microfluidic device specifically designed for water-window microscopy. By applying controlled AC fields, our microfluidic flow cell (MFC) allows trapping and orienting the cells without the need for complex or restrictive fixation methods.

We validated this approach by combining our microfluidic system with a compact, previously described laboratory-based correlative SXR/fluorescence microscope.[35] This work highlights the potential of our platform to advance biological SXR microscopy toward more versatile and physiologically relevant applications.

Results

Microfluidic and optical setup

As illustrated in Fig. 1, the experimental system consists of three main components: microfluidics, electronics, and the correlative microscope, with most parts placed inside a vacuum chamber. Inside the chamber, an MFC holds the microfluidic chip, which features silicon nitride (Si_3N_4) windows, transparent to SXR, hence enabling microscopy in the water window spectral region.

The fluidic system outside the vacuum chamber includes two different pumps: a pressure-driven pump and a syringe pump, alternatively used at different moments during the sample injection. The pressure-driven pump regulates the flow rate of the sample, containing the target cells and buffer solutions. Once the sample is inside the microfluidic chip, the syringe pump enables the precise movement of small sample volumes to stabilize the position of the single cell within the field of view. A computer interface synchronizes both fluidic and dielectrophoretic control and ensures precise handling of the sample throughout the system. The tubing from the pumps is introduced into the vacuum chamber through a dedicated inlet feedthrough, reaching the flow cell connector (highlighted in green in Fig. 1). A second connector (highlighted in red in Fig. 1), placed on the opposite side of the flow cell, directs the waste fluid toward

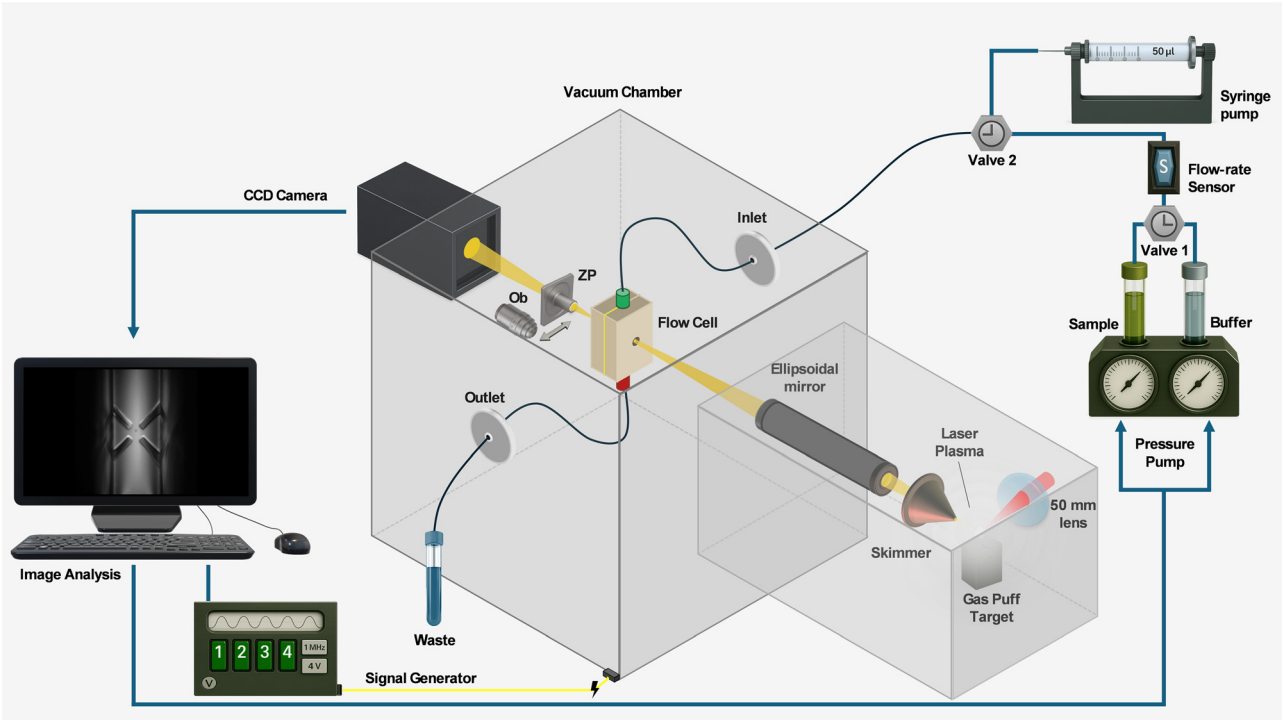

Fig. 1 Schematic overview of the microfluidic system and the SXR microscope (not to scale). SXR microscopy requires a vacuum chamber in which all microscope components, including the MFC, are placed. A pressure pump regulates the introduction of either the sample or the buffer solution, selected *via* valve 1. The flow rate is monitored in real time by a dedicated sensor. Alternatively, the sample can be injected using a syringe pump, allowing precise introduction of small volumes during the cell trapping phase; valve 2 switches between the two injection methods. The flow is directed through tubing to the inlet feedthrough, enters the flow cell *via* the green connector, passes through the microchip, and exits through the red connector on the opposite side, reaching the outlet feedthrough and finally the waste collection tube. System operation is controlled *via* a computer interface, which manages the pump cycles, and a signal generator powering the electrodes embedded in the microchip. These electrodes enable cell manipulation *via* negative dielectrophoresis (nDEP), monitored optically in real time. The cell suspension flowing through the chip is imaged either *via* a visible light microscope or the soft X-ray microscope, by alternately bringing the objective lens (Ob) or the zone plate (ZP) into position. The schematic shows the system in SXR mode, with the ZP imaging the sample structure onto the detector. In this configuration, the fluorescence microscope is inactive. After imaging, the system can be flushed with ultrapure water, and the sample vial can be replaced with one containing a different microorganism, allowing a new analysis to be performed without altering any other component of the setup. The image is based on the sketch in ref. 35.

the outlet feedthrough disposing it in an external waste vial. An additional feedthrough is included to enable the necessary electrical connections.

The correlative microscope has been described and characterized previously.[35] It enables alternating inspection *via* either SXR imaging or visible light (VIS) microscopy. In the latter case, the selective use of optical filters allows for a transition between fluorescence microscopy and quasi-brightfield imaging in reflection, facilitating the real-time monitoring of channel filling and cell trapping. To enable SXR imaging, a laser-generated plasma source is employed, using nitrogen as the target gas to produce monochromatic SXR line emission at 2.88 nm (configuration shown in Fig. 1). The emitted light is collected by an ellipsoidal mirror, which acts as a condenser to illuminate the specimen. The sample is imaged by a Fresnel zone plate, serving as the objective lens of the SXR microscope, onto a CCD camera. Once the experiment is concluded, the visible light objective returns to its initial position, to inspect the sample again and prepare the system for subsequent experimental phases.

Flow cell and microfluidic chip

The microfluidic chip is embedded inside a microfluidic flow cell (Fig. 2) which provides both fluidic and electrical connections required for sample handling and optical analysis. It was specifically designed to operate under vacuum conditions, using materials with low outgassing rates to prevent contamination, and has been shown to maintain a stable pressure of at least 10^{-5} mbar within the vacuum chamber. In particular, the flow cell was made of polyether ether ketone (PEEK), a high-performance thermoplastic known for its excellent mechanical properties, chemical resistance, and thermal stability. For the electrical connections, spring-loaded pins were inserted through dedicated slots in the MFC, establishing contact with the electrodes on the chip frame surface. As shown in Fig. 2a, the microfluidic chip consists of two commercially available silicon frames each measuring 23.5 × 23.5 mm^2 and containing free-standing 150 nm-thick Si_3N_4-membranes at their centers. These membranes serve as windows for SXR

 This journal is © The Royal Society of Chemistry 2026

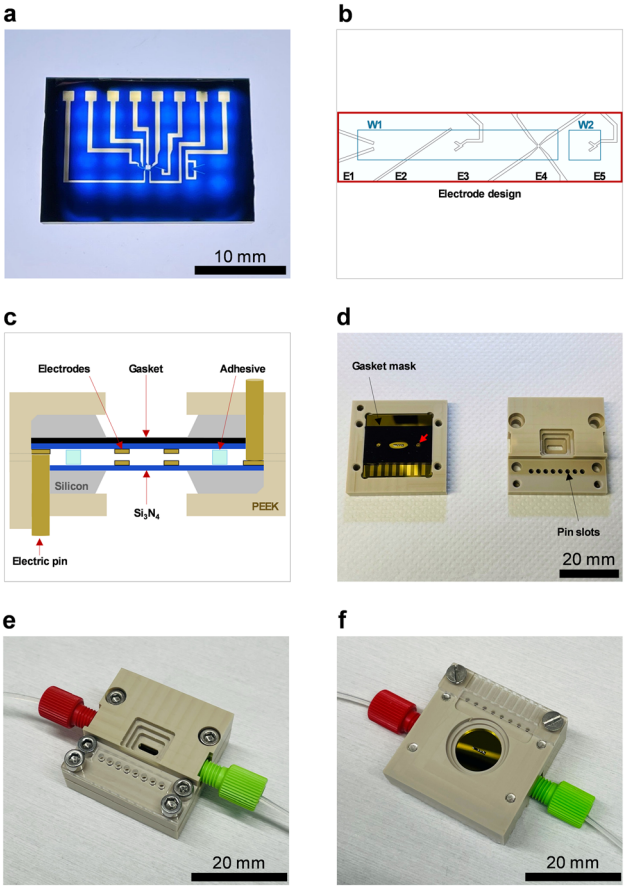

Fig. 2 MFC components. (a) Individual silicon frame coated by a thin Si_3N_4 layer, featuring custom-designed gold electrodes and windows for VIS and SXR imaging. (b) Schematic representation of the Si_3N_4 membrane windows: W1 (rectangular) and W2 (square). The electrode layout is also shown, featuring five distinct structures: E1, the funnel for particle alignment; E2, the deflector for trajectory control; E3 and E5, the hook-shaped electrodes for stopping particles; and E4, the field cage designed for high-stability trapping of particles. (c) Cross-section view of the fully assembled flow cell, showing the adhesive bonding layer, the alignment between the two complementary frames forming the microchip, and the optical openings in the housing. (d) Left: FKM gasket mask used for sealing, exposing the central window region and microfluidic access holes (red arrowhead). Right: Slots for the electrical contact pins. (e) Assembled MFC, including the electrical pin interface and microfluidic connectors. (f) Imaging side of the MFC.

transmission. Each frame holds two windows measuring 50 × 850 μm and 50 × 50 μm, respectively. To enable dielectrophoretic control, custom-designed planar gold microelectrodes were photolithographically patterned on top of both the free-standing membranes and the surrounding Si_3N_4-coated silicon frame (Fig. 2b). The photolithography process was carefully optimized to account for the different reflectivities and thermal properties of silicon-supported and free-standing Si_3N_4. Note that the fabrication of the silicon support frames and Si_3N_4 membranes was not part of this study. The general octupole DEP field-cage concept was adapted from previously reported work.[41–44] The device-specific contribution reported here is the implementation of this concept on two opposing SXR-transparent Si_3N_4 membrane frames and its integration into a vacuum-compatible microfluidic flow cell.

The schematic in Fig. 2c shows a cross-section of the assembled MFC. The two frames were bonded together using a pressure-sensitive adhesive, with a thickness of 10 μm, which defines the internal microfluidic channel. The scheme highlights the position of the gold electrodes on the Si_3N_4 window, aligned with the upper and lower openings of the MFC to allow optical access. To ensure effective sealing, a gasket mask made of FKM (Fluorine Kautschuk Material, a vacuum-compatible fluoroelastomer material) was placed between the microchip and the flow cell. This gasket mask had only three small apertures to allow access to the Si_3N_4 membranes and the fluidic interfaces (Fig. 2d).

Fig. 2e shows the fully assembled MFC, highlighting the front slot for electrical pins and the lateral microfluidic connectors. The back of the MFC (Fig. 2f) features a large circular aperture designed to allow the X-ray microscope's zone plate to be positioned in close proximity to the chip surface.

Single-cell trapping mechanism and consecutive sample analysis

A schematic representation of the single cell trapping mechanism is illustrated in Fig. 3a. The sample, suspended in solution, is transported by pressure-driven flow from the inlet to the outlet, passing through the inspection field on the silicon nitride windows, which are the only transparent areas of the chip. By shifting the MFC vertically, it is possible to inspect different areas of the silicon nitride windows, thereby enabling the tracking of the single cell trajectory along the microchannel.

Cell control and positioning within the microchannel are driven by dielectrophoresis (DEP). DEP describes the motion of a polarizable object in a spatially nonuniform electric field. The device was operated in the negative DEP regime, in which cells and particles are displaced away from regions of high electric field strength and towards an electric field minimum. A detailed description of this mechanism has been provided in previous studies.[45–52]

The three-dimensional nonuniform electric-field distribution required for DEP control is generated by gold microelectrode structures patterned on the opposing upper and lower Si_3N_4 membranes and driven with phase-controlled signals. This arrangement produces field gradients in both the lateral and vertical directions of the microchannel, enabling three-dimensional cell manipulation. The electrode layout combines upstream transport control with a central three-dimensional trapping region. All the electrodes of the chip are arranged in pairs on the upper and lower surfaces of the channel and are powered by a square-wave radiofrequency signal (1 MHz), with voltages of about 3 V. Along the flow direction, cells encounter a sequence of electrode pairs with distinct

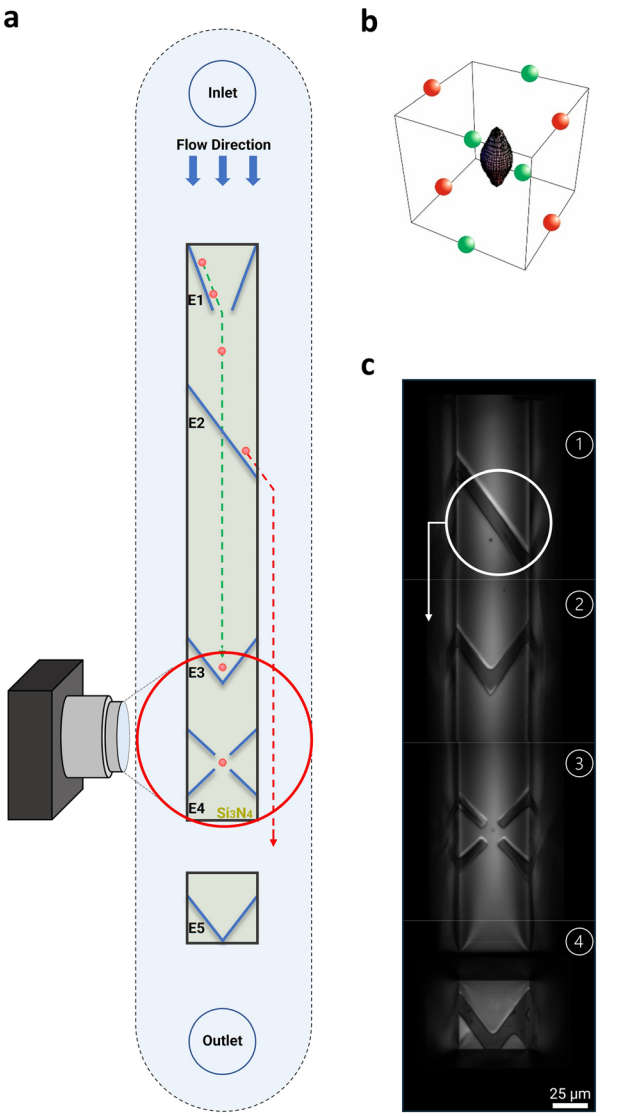

Fig. 3 Single cell trapping mechanism. (a) Schematic representation of the microfluidic channel, which is partially observable *via* VIS microscopy only at the locations corresponding to the Si_3N_4 membrane windows. A cell suspension introduced into the flow cell is directed through the channel by a sequence of electrode pairs (labelled E1–E5). Electrode pair E1 focuses the cells toward the center of the channel, forming a single-cell stream. Non-target cells are diverted by E2 (red trajectory), while target cells proceed toward E3 (green trajectory). Subsequently, individual target cells can be trapped either in the main field cage (E4) or in the hook-shaped electrode. (b) Schematic of the field cage region under nDEP activation, showing the field minimum and the confining potential within the field cage. Electrodes are symbolised by spheres, the colors of which indicate the phase of the applied electric field (0° – green, 180° – red). Image adapted from Duschl *et al.* (c) Composite VIS image obtained by combining 4 adjacent fields of view acquired along the axial direction, corresponding to four distinct regions of the microchannel associated with electrode pairs E2–E4. The individual fields were sequentially recorded by vertically translating the MFC using the motorized stage inside the vacuum chamber, allowing visualization of the different functional zones involved in the imaging workflow: 1 – the deflection electrodes (E2), 2 – the first hook electrode (E3), 3 – the central field cage used for stable trapping (E4), and 4 – the second hook electrode (E5).

geometries and functions: focusing, deflection, temporary retention, and trapping.

The first electrode pair (E1) focuses the cells at the center of the channel, aligning them along the midplane and directing toward the next electrodes (dashed green trajectory in Fig. 3a). The transverse electrodes (E2) act as a barrier and are activated to selectively deflect non-target cells, excluding them from the imaging area and guiding them toward the outlet for disposal (dashed red trajectory in Fig. 3a). When a target cell is identified, the hook-shaped electrode pair (E3) is activated to trap it. This electrode geometry acts as a barrier that ensures effective holding. Once the cell is stable, the flow is gradually reduced and the potential of E3 is progressively lowered, allowing precise and controlled transition of the target cell into the activated field cage (E4). The field cage electrodes represent the core component for further SXR analysis as it enables the accurate and contactless trapping of single cells. They are arranged as an octupole of eight independently addressable electrodes, with four electrodes patterned on each Si_3N_4 membrane. Under nDEP conditions, the phase-controlled excitation creates a three-dimensional electric-field minimum near the center of the cage[53] (Fig. 3b), thereby providing contactless confinement of the cell. Adjusting the relative phase and amplitude of individual electrode signals shifts this field minimum and enables controlled repositioning of the trapped cell within the accessible trapping volume at the nanometric scale. As a result, the sample can be trapped with no need for adjustments over more than 10 hours. Once the cell is stably trapped, SXR imaging is performed and after the image acquisition, the particle is released.

Fig. 3c shows the reconstructed view of the microfluidic channel regions containing the Si_3N_4 membranes, obtained by combining four distinct VIS image acquisitions when moving the MFC.

By increasing the flow rate and deactivating the electrodes, the sample is finally expelled and directed into the external waste vial. The microchannel is flushed and is ready for the next acquisition run, which can proceed without venting the system, enabling rapid consecutive sample analysis through simple replacement of the external reservoirs.

Trapping stability

As shown in Fig. 3b, the cage generates a three-dimensional dielectric force potential that confines the particle. Trapping stability was evaluated for polystyrene microparticles and eukaryotic cells (see the SI). Trapping accuracy within this potential is defined as the spatial displacement of the object from its central position along the x and y coordinates while it is held stationary inside the cage.

To conduct the stability test, it is essential to define the "trapping mode", as defined by Duschl *et al.*[50] The modes refer to the phase differences between the eight electrodes that form the octupole, which minimizes the variance of the equilibrium position. The most efficient trapping mode C

This journal is © The Royal Society of Chemistry 2026

consists of a 180° phase difference between adjacent electrodes, with opposite (top and bottom) electrodes sharing the same phase. With this phase distribution, a confined electric field is established, ensuring the best trapping stability with the particle positioned exactly at the center of the internal volume of the field cage, equidistant from the eight electrodes. This configuration was employed throughout the experiments conducted in this work, with the electric field frequency consistently set at 1 MHz.

For the test, samples of single Jurkat cells and polystyrene microparticles were trapped within field cages according to the identified configuration. Using bright-field microscopy, images were acquired at regular intervals. The images were automatically post-processed to locate the center of each particle. The coordinates were then statistically analyzed to estimate the displacement. A more detailed explanation and comparison between phase configuration modes are provided in the SI. For a 30 μm × 30 μm octupole field cage (diagonal tip-to-tip × vertical spacing), operated in mode C at voltages between 3 and 5 V (to ensure cell viability), positional stability was better than 50 nm, which corresponds to the resolution limit of our optical tracking method.

System validation and functional characterization

To assess the functionality of the setup before the SXR analysis, a validation procedure was conducted focusing on pressure stability, microfluidic sealing and DEP performance. An overview of the main processes involved in the experiment over 10 days is presented in Fig. 4. The first step involved integrating the MFC in the vacuum chamber at the focal position of the SXR microscope. This included establishing fluidic and electronic connections and aligning it with optical components. Subsequently, the chamber was evacuated to a pressure of 10^{-5} mbar, and pressure stability was monitored to ensure proper sealing. To further validate the system's integrity (system test, Fig. 4), ultrapure water was introduced into the flow cell, while simultaneously monitoring the pressure and flow rate sensors to confirm consistent flow. The fluidic test was performed at increasing flow rates over 24 hours, demonstrating stable pressure inside the chamber and confirming the absence of leakage.

When the MFC is placed under vacuum for SXR imaging, a significant pressure difference arises between the internal liquid-filled channel and the external vacuum environment.

This pressure differential leads to mechanical deformation of the thin Si_3N_4 membranes, increasing the thickness of the enclosed water layer and thereby reducing transmission in the water-window spectral range. Particularly in larger-window configurations, this membrane bending can become substantial and compromise imaging performance.

To quantify this effect, the vertical spacing between the membranes was experimentally measured at different window geometries by using the zone plate of the SXR microscope, which is mounted on a closed-loop piezo stage and features a small depth of focus (~1 μm).

The focal plane was first adjusted to the electrodes on the bottom membrane and then to the top membrane (Fig. 5),

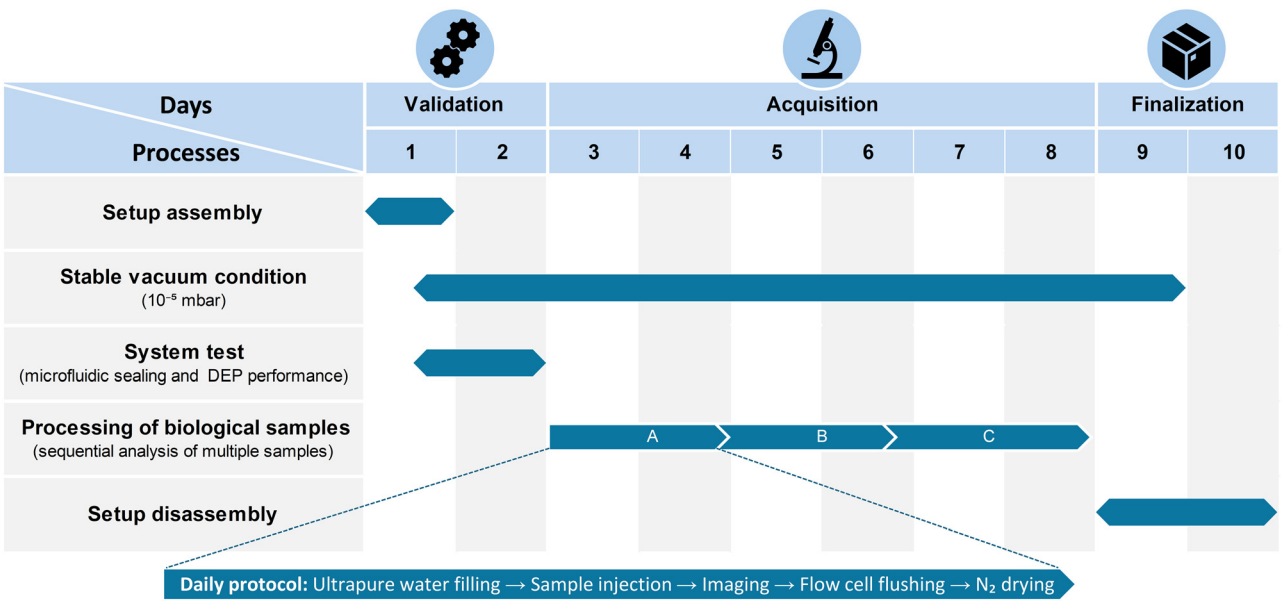

Fig. 4 System validation processes. The diagram shows the main steps of the experimental workflow in relation to the timeline (in days). Following assembly, the vacuum chamber was sealed, and the system was prepared to reach the working pressure conditions required for SXR microscopy. These vacuum conditions were maintained throughout the entire experimental period, spanning 9 days. Initial validation included verifying the proper sealing of the flow cell and assessing the functionality of the DEP system by introducing a suspension of 3.5 μm polystyrene microparticles into the microfluidic channel and confirming effective electrode operation. Subsequently, without interrupting the experimental workflow, distinct biological samples were sequentially introduced into the system, and each was subjected to SXR exposure for imaging. Finally, the vacuum chamber was gradually vented back to atmospheric pressure, and the experimental apparatus was disassembled as planned.

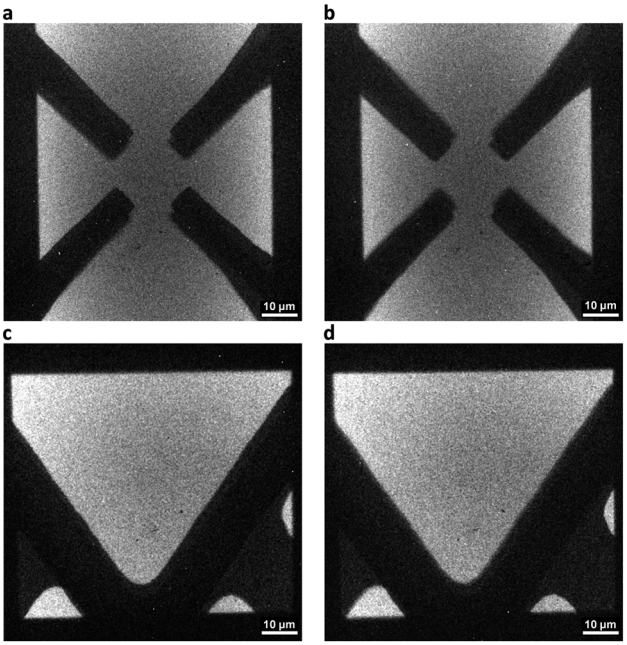

Fig. 5 SXR transmission images of two membrane windows under vacuum conditions with panels (a) and (c) focused on the electrodes of the top membrane and panels (b) and (d) on those of the bottom membrane. (a) and (b) Detail of the larger rectangular window containing the cage region; membrane bending results in a water layer thickness of 21 ± 1.5 μm. (c) and (d) Image of the smaller square window containing the second hook electrode. The bending is significantly reduced, with a water layer thickness of 12 ± 1.5 μm. All images were acquired with total integration times of approximately 20 minutes. In all cases, transmission is reduced toward the center of the window due to increased water thickness resulting from membrane deformation.

allowing precise determination of the water column thickness, which was designed to be 10 μm. For the larger rectangular window, where the cage was located, the water layer thickness was measured to be 21.0 ± 1.5 μm. In contrast, the smaller square window, featuring the secondary hook, showed significantly less bending, with a thickness of 12.0 ± 1.5 μm.

Moreover, measurements and SXR images consistently revealed that membrane bending is inherently not uniform across the window. The water column is thicker at the center than at the edges, a result confirmed both by focusing measurements and by the brightness distribution in the SXR images. In all images, the central region appears darker, consistent with increased absorption due to greater water thickness.

Analysis of test samples and different biological samples in series

To assess the proper functionality of the electronic components, polystyrene microparticles (diameter 3.5 μm) were introduced into the system (system test, Fig. 4), validating their correct manipulation through nDEP. The successful dielectrophoretic trapping in the field cage was confirmed through VIS microscopy (Fig. 3c) and subsequently SXR imaging was performed.

To achieve uniform illumination, the MFC was centered in the beam path. Fig. 6 shows VIS images and SXR images of a polystyrene microparticle and different biological samples in a solution of water and PBS, trapped within the field cage. All SXR images are the sum of individual frames with shorter exposure times (120 s for the polystyrene microparticle and 210 s for biological samples). To mitigate systematic drift, a series of short exposures were acquired. Each individual frame was corrected for drift by determining its spatial displacement *via* cross-correlation of a distinctive region of interest (ROI) against a reference image (*e.g.*, the first or last frame of the series). These aligned frames were then co-added, yielding a single combined image with an effective long integration time (detailed in Reinhard *et al.*[35]). An effective integration time of at least 1 hour per image was necessitated by the increased water layer thickness of approximately 21 μm (caused by membrane bending).

Fig. 6a shows the microbead. Prior to SXR imaging, VIS microscopy was used to verify the sample position. The corresponding SXR image displays a sharply defined bead, confirming its positional stability within the spatial resolution of the system.

Following this initial validation with fluorescent microbeads, the system was used in a series of experiments with three different biological samples (Fig. 6b–d), all introduced without venting the vacuum.

Between each analysis, the system was flushed with ultrapure water to remove the residual material from the microfluidic channel before loading the next sample. Under the conditions used in this study, this procedure enabled the consecutive analysis of the reported samples. Sample preparation consisted simply of dilution in PBS solution and water, resulting in a final cell concentration of approximately 10^5 cells per mL.

The tested samples included various phylogenetically diverse photosynthetic microorganisms, *e.g.*, the unicellular freshwater cyanobacterium *Synechocystis* sp. PCC 6803, a widely used model organism for photosynthesis and molecular biology, *Tisochrysis lutea* RCC 1349, a marine haptophyte of ecological and biotechnological interest, and *Chlamydomonas euryale* SAG 25.89, a flagellated eukaryotic microalga often employed in studies of motility and light response.

SXR imaging was performed, and the resulting images are shown in Fig. 6b–d. During the analysis, intervals were taken to conduct inspections using the integrated fluorescence microscope, in order to monitor the cellular state. All samples were imaged by acquiring a large number of short-exposure frames (210 s per frame). These frames were drift-corrected and summed to generate a final image with a substantially longer effective integration time. The total measurement duration for a typical biological sample was approximately 3 h. However, because some of the trapped cells exhibited gradual motion during the initial phase of the

 This journal is © The Royal Society of Chemistry 2026

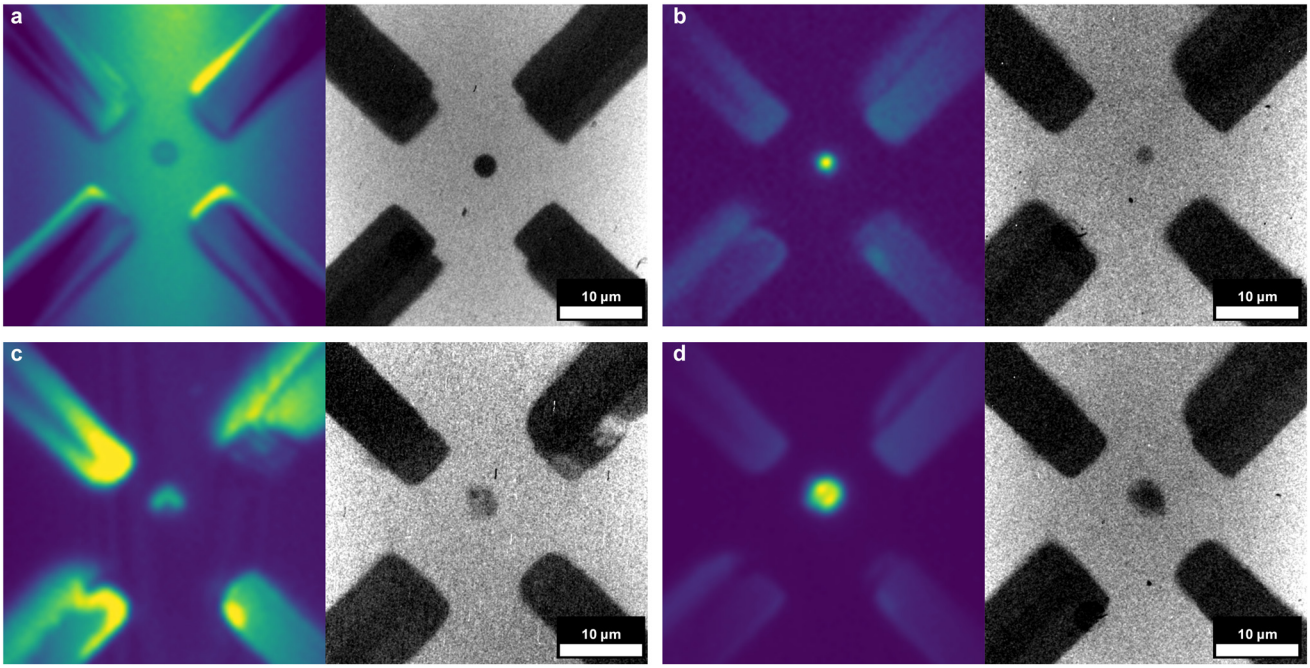

Fig. 6 Imaging of different biological samples trapped within the MFC using VIS (left) and SXR microscopy (right). (a) Brightfield image (left) and SXR image (right) of a polystyrene bead used for system validation, stably trapped and clearly visible in both imaging modalities (exposure times 5 ms bf, 2 h SXR, no binning). (b) *Synechocystis* sp. PCC 6803 cell, stably trapped and imaged *via* chlorophyll autofluorescence with an exposure time of 50 ms (left); corresponding SXR image with a total integration time of 1.25 h (right). (c) *Tisochrysis lutea* RCC 1349, SXR image (right, total integration time 1.25 h) and fluorescence image (left, exposure time 100 ms). (d) *Chlamydomonas euryale* SAG 25.89, SXR (right, total integration time 1 h) and fluorescence (left, exposure time 50 ms).

experiment, only the final 60 min data were retained for the imaging. Fig. 6b shows a single cell of the cyanobacterium *Synechocystis* sp. PCC 6803. The cell was stably trapped and remained in position throughout the imaging process demonstrating the suitability of the MFC for handling delicate biological specimens under vacuum conditions. In the fluorescence image (left), the cell appears as a bright, compact spot due to autofluorescence from chlorophyll *a*, which is contained in thylakoid membranes characteristic of photosynthetically active cyanobacteria. The corresponding SXR transmission image (right) shows a localized increase in absorption at the same position. This result highlights the ability of the MFC to maintain cell integrity and position during imaging, while enabling simultaneous acquisition of functional and structural information.

Fig. 6c shows *Tisochrysis lutea* RCC 1349, a flagellated microalga. In the fluorescence microscopy image (left), the cell exhibits an apparent triangular or lobed morphology. In the corresponding SXR transmission image (right), this structure is hardly visible because persistent flagella-driven motion during the relatively long total exposure time of 210 s per frame caused substantial blurring and loss of structural detail. Nevertheless, three distinct regions of higher absorption are apparent, which may correspond to denser subcellular compartments. This observation highlights a challenge for DEP trapping of highly motile organisms in the present configuration: although the platform successfully confined the cell within the imaging area, the residual mobility currently limits full immobilization for high-resolution soft X-ray imaging at long exposure times.

Fig. 6d shows *C. euryale*, the third alga trapped during the same vacuum session using our flow cell. The cell also was in motion during imaging, although it remained confined by the DEP field cage. In the fluorescence image (Fig. 6d – left), the cell displays an elongated, asymmetric shape with a pointed anterior end which is consistent with the known morphology of *C. euryale*. While finer structural details are blurred or cannot be resolved because of the cell's persistent motion during image acquisition, a similar overall shape is preserved in the corresponding SXR transmission image (right).

Discussion

The developed system allows imaging of suspended single cells in their native liquid environment using SXR microscopy in the water window range. As illustrated in Fig. 1, the integration of microfluidics with SXR microscopy, combined with the use of nDEP for contactless cell manipulation, has enabled the imaging of cell suspensions while preserving the cell's structural integrity within the limits of experimental observation.

The hydraulic sealing between the flow cell and the microchip is mechanically achieved by compressing a gasket. This feature is essential to guarantee the system's suitability for long-term operation in vacuum environments. A central

requirement for the intended application is that the flow cell maintains both vacuum integrity and liquid confinement throughout extended imaging campaigns. Fig. 4 presents a timeline of the full series of consecutive experiments, spanning 9 days and multiple samples. Over this period, the chamber pressure remained stable in the low 10^{-5} mbar range, with no measurable drift or venting events between sample exchanges. This sustained pressure stability, maintained across repeated sample transfers without breaking vacuum, demonstrates the effectiveness of the sealing scheme and confirms that the device meets the vacuum requirements of water-window SXR microscopy. The stable chamber pressure indicates that no major leakage event occurred during the measurement campaign. However, liquid loss was not quantified directly, and small losses below the pressure-detection limit cannot be excluded. Furthermore, the compatibility of the present operating conditions with more sensitive biological samples was not systematically assessed. Sample-specific effects of the buffer composition, exposure duration, and SXR irradiation therefore require validation in future applications. The extended duration of the experiment was facilitated by the practical design of the setup, which allows for sample loading without the need to open the vacuum chamber. This rapid in-vacuum sample transfer capability is a key distinguishing feature of the present work.

An important aspect to consider is the pressure difference between the inside of the microchannel and the external environment of the silicon nitride windows. Particularly under vacuum conditions, this difference can deform Si_3N_4 membranes, increasing the thickness of the water column and compromising X-ray transparency within the water window spectral range. The use of two small-area windows proved to be effective in mitigating this effect by reducing membrane bending compared to larger-window configurations. The distances between the membranes were experimentally measured at each Si_3N_4 window (Fig. 5) and found to be 21 μm and 12 μm for the rectangular and the square window, respectively.

These findings have direct implications for future device design. Less membrane bending, corresponding to a thinner water layer, allows for shorter exposure times and improved imaging contrast. For this reason, the cage should be positioned in a separate, smaller window, accepting reduced operational overview and handling convenience when transferring particles between the hook and cage. Other possible mitigation strategies include the integration of membrane support features or the increase of membrane thickness, which would result in less bending. However, thinner membranes remain attractive, as the transmission is for example only $T = 13.3\%$ for 300 nm Si_3N_4.

It should also be noted that non-uniform membrane deformation may introduce spatially varying attenuation, which must be considered in any quantitative image analysis based on SXR transmission. As demonstrated in the experimental results (Fig. 3c), this spatial variation is directly observable in VIS microscopy, where the center of the membrane window appears brighter than the edges. This effect results from membrane curvature: at the center, where the surface is closer to normal with respect to the optical axis, more light is reflected into the objective. Toward the edges, steeper surface angles reduce the amount of light collected by the objective lens. The same curvature leads to a locally increased water path length in the central region, significantly exceeding the nominal channel thickness of 10 μm and resulting in an approximately sevenfold increase in SXR absorption.

We further characterize the intrinsic stability of object trapping in an octopule cage configuration (Fig. S1 and S2 in the SI). These experiments were carried out under ambient conditions in a 30 μm-high channel using polystyrene microparticles and Jurkat cells as model systems. The purpose of this analysis was to determine optimal cage geometries and electric-field parameters that maximize trapping stability by generating dielectrophoretic forces that effectively counterbalance gravity, medium viscosity, and Brownian motion, thereby limiting the particle's positional variation below the 50 nm resolution limit of the microscope employed. Under optimal conditions, the cell is robustly held at the center of the field cage, equidistant from the eight electrodes, and exhibits minimal oscillations around its equilibrium point. The measured positional variation around the central position of 50 nm reflects the resolution limit of our optical tracking method and therefore represents a conservative lower bound for the achievable trapping stability.

Note, however, that the dimensions of the cage and microchannel for SXR imaging were slightly different from those employed in the stability test. The SXR experiments presented in this work were conducted in a channel with a nominal height of 10 μm, corresponding to an effective liquid-layer thickness of approximately 21 μm under vacuum due to membrane bending. For identical voltage amplitudes, the reduced electrode spacing increases the electric-field gradient and thus the dielectrophoretic force, so that at least comparable, and likely improved, translational stability can be expected.

The integration of brightfield or fluorescence imaging in the SXR microscope is crucial for real-time monitoring during cell selection and positioning within the microchannel, enabling precise handling and trapping of single cells. Fluorescence imaging further facilitates the distinction between biological targets and non-specific residues (*e.g.*, from the growth medium), which is often not possible with brightfield imaging alone. Once trapping is completed, the system was switched to the SXR microscopy mode, through alignment of the zone plate with the flow cell opening. In the future, the system could be simplified by employing impedance-based detection using integrated electrodes instead of optical monitoring of the particle position, thereby omitting the need for a hybrid VIS/SXR microscope.

 This journal is © The Royal Society of Chemistry 2026

As shown in Fig. 4, after validating the operational conditions of pressure and fluidic stability, a suspension of polystyrene microparticles was introduced to verify the effectiveness of the trapping system. The particles responded as expected to the dielectrophoretic configuration, allowing successful trapping of a single particle for further SXR imaging. Continuous flow can, in principle, reduce radiation damage by removing radiolysis products and free radicals from the liquid. However, systematic evaluation of different flow conditions demonstrated that the field cage achieves the highest trapping stability, and therefore the best image contrast, when operated under no-flow conditions. In the absence of hydrodynamic forces, the dielectrophoretic force generated by the eight-electrode field cage can more effectively counterbalance gravity, resulting in improved positional stability of the trapped particle. In contrast, the application of continuous flow, even at moderate rates, was found to degrade image quality, most likely due to flow-induced oscillations, particularly along the vertical axis aligned with the gravitational force. For these reasons, in this work a low basal flow rate was maintained during sample handling, while the flow was consistently interrupted during SXR image acquisition to maximize trapping stability and imaging performance.

It is important to highlight that characterizing the system using polystyrene beads allowed us to identify the optimal working conditions, which can be transferred to biological samples. However, this step is not necessary for future experiments once the optimal conditions are known.

The final achievement in this work was the consecutive analysis of three different microorganisms in one single vacuum session along several consecutive experimental days. The imaging was performed as a sequence of short exposures, each individually corrected for drift prior to co-addition. The image of an ~2.5 μm *Synechocystis* cell (Fig. 6b) highlighted stable trapping and good contrast with non-motile objects. This observed size is in agreement with typical dimensions reported in the literature.[54] Due to its compact morphology and the absence of flagellar motion, this cyanobacterium remained stably positioned throughout the image acquisition. The autofluorescence from chlorophyll *a* provided a clear signal for identification and correlated well with the high absorption contrast in the SXR image, indicating internal structural density. Fig. 6c and d, related to *Tisochrysis lutea* and *Chlamydomonas euryale* (diameter >5 μm), show reduced edge definition, attributable to the residual motility observed under VIS, likely caused by flagellar activity not fully compensated by the dielectrophoretic field. Over the total acquisition period of approximately three hours, a progressive improvement in image quality was observed. During the initial phase, residual motion of the specimen within the DEP cage introduced blurring, whereas this motion diminished substantially over time and was markedly less pronounced during the final hour. We attribute this behaviour to the gradual decline in cell viability under prolonged X-ray exposure, which progressively suppressed motility. Within the DEP cage, the dielectrophoretic forces are sufficient to translationally confine the specimen but do not fully suppress motional degrees of freedom in viable, motile organisms. The observed reduction in motility is therefore biological in origin rather than a consequence of increased trapping force. For future experiments, cells could be loaded into the system, exposed to SXRs for imaging, and subsequently recovered from the flow cell to evaluate their viability by monitoring their regrowth under standard culture conditions. It is worth noting that highly motile organisms such as flagellated microalgae require additional sample preparation, for instance deflagellation or optimization of buffer conditions to suppress motility in order to be fully compatible with the long integration times of the current SXR setup. However, optimizing imaging performance was beyond the scope of this work. Instead in this study, these specimens were used solely as readily accessible proof-of-concept samples to verify stable DEP trapping under vacuum, confirming that the flow cell provides sufficient X-ray transmission for interpretable SXR imaging, and demonstrate rapid sample exchange without venting the vacuum, rather than to benchmark or optimize imaging performance.

Overall, the results confirm the effectiveness of the system in enabling SXR imaging of single cells under native conditions, while providing important insights into the key factors influencing sample stability and final image quality. A key and distinctive feature of the platform is its sample transfer capability, enabling successive analysis of different specimens using a single setup. Unlike static liquid cells or cryo-fixation approaches, which require disassembly or venting between measurements, our system enables rapid and consecutive specimen exchange without breaking the vacuum. This constitutes the primary advance of this work as the first realization of a vacuum-compatible rapid sample-transfer system for SXR microscopy.

Besides structural snapshots, the platform also opens the door to stimulus response experiments at the single-cell level. Because the microfluidic system allows direct delivery of chemical stimuli such as ions, nutrients, signaling molecules, toxins, or interacting cells to a stably trapped specimen, it opens the possibility of sequential SXR imaging before and after controlled perturbation. Such experiments could provide insights into slow structural adaptations at the subcellular level, including stress responses, organelle reorganization, and host–pathogen interactions. The total acquisition period (1–3 h) limits this approach to relatively slow processes; however, improved photon flux and reduced liquid thickness are expected to lower required acquisition times and therefore broaden the range of accessible biological dynamics. Combined with integrated VIS/fluorescence microscopy, suitable target cells can be identified and selected prior to SXR imaging, enabling efficient consecutive analysis of structural and morphological changes across different conditions.

Future developments of the system could focus on enabling operation with coherent light source microscopes, or even synchrotron-based setups. The modular design of the flow cell makes it highly versatile and potentially compatible with advanced SXR techniques, such as tomography, thereby maximizing the benefits of SXR imaging to achieve nanometric spatial resolution. Besides translational trapping, octupole field cages of the type used here have previously been shown to enable controlled rotation of trapped cells about arbitrary axes under ambient conditions.[48–50] Although not implemented here, this suggests a possible route toward *in situ* tilt-series acquisition for SXR tomography. Demonstrating this will require calibrated, drift-free rotation within the thin liquid layer at acceptable radiation dose, which remains the subject of future work. Likewise, it could also facilitate seamless integration with other imaging techniques, such as ptychography[55] and X-ray diffraction. Ultimately, radiation damage will limit the achievable resolution by SXR imaging on hydrated samples. Recent theoretical studies[56] have indicated that, under optimized conditions, resolutions down to ~20 nm could be achieved with radiation doses at the Henderson limit, beyond which radiation-induced chemical damage, including bond breaking, mass loss, and free-radical formation, degrades image quality. Recent experimental demonstrations of hydrated state ptychography in the water window have achieved ~60 nm resolution.[57] Further optimization of contrast, data acquisition, and image deblurring may enable additional advances toward higher resolution. In this context, implementing controlled fluid flow between image acquisitions could help mitigate radiation damage by flushing away harmful radicals produced by SXR radiation, thereby enhancing dynamic, three-dimensional and high-resolution imaging of biological samples in suspension under SXR illumination.

Experimental

Dielectrophoretic cell handling and DEP field cage

All DEP electrodes were driven with square-wave signals at a fixed frequency of 1 MHz. The paired deflection electrodes were operated with a phase difference of 180°.

The DEP field cage consisted of eight independently addressable electrodes, with four electrodes patterned on each of the two opposing Si_3N_4 membranes.[41–44] The field cage was operated in mode C (see the SI), with laterally adjacent electrodes driven with a 180° phase difference and opposing electrodes on the upper and lower membranes driven in phase.[50] DEP signals were applied at 3–5 V_{rms}, depending on the experimental conditions.

X-ray transparent microfluidic chip fabrication

The X-ray transparent microfluidic chips were fabricated by assembling two commercial silicon frames (23.5 × 23.5 mm^2, 381 μm thick) bearing Si_3N_4 membrane windows. Gold electrodes for DEP manipulation were patterned on the membrane surfaces (μPG 101, Heidelberg Instruments, Germany). Before metallization, the frames were cleaned in ultrapure water and isopropanol, dried under N_2, and treated with oxygen plasma to remove organic contaminants and improve metal adhesion. A chromium adhesion layer (~7 nm) followed by a gold layer (~70 nm) was deposited by physical vapor deposition (Auto 500, BOC Edwards, UK). Electrode patterns were defined by standard photolithography (μPG 101, Heidelberg Instruments, Germany) using a positive photoresist (AZ 1514 H, MicroChemicals GmbH, Germany), followed by wet chemical etching of gold and chromium. After etching, the residual photoresist was removed by alkaline treatment and solvent rinsing, resulting in clean and well-defined electrode structures on the Si_3N_4 membranes.

The silicon frames were mechanically customized to enable fluidic and electrical interfacing. One frame was laser-cut to introduce inlet and outlet ports (0.8 mm diameter), while the outer geometry of both frames was trimmed to fit the dedicated internal pocket of the flow-cell. The final microfluidic chip was assembled by bonding two complementary frames face-to-face, with the electrode-patterned sides oriented inward and a 10 μm-thick pressure-sensitive adhesive spacer (No. 5601, Nitto Denko) positioned between the frames to define the microchannel geometry. Alignment of the upper and lower electrode structures was achieved by inspection under an optical microscope (IX71, Olympus Corporation, Japan), followed by the application of uniform mechanical pressure to seal the device. The overlap of the upper and lower membranes defined the effective imaging region enabling VIS and water-window SXR microscopy under vacuum-compatible liquid-phase conditions.

Microfluidic system and flow control

The microfluidic system was designed to enable reliable fluid handling and precise flow control within the SXR microscope vacuum environment. Fluid delivery to the flow cell was achieved using vacuum- and chemically compatible microfluidic fittings (Super Flangeless TechLab, Germany) and fluorinated ethylene propylene (FEP) tubing (1527 IDEX, USA), ensuring stable operation under vacuum conditions. Adhesively mounted vacuum feedthroughs enabled the connection of the microfluidic tubing to the MFC inside the vacuum chamber, providing a leak-tight interface between atmospheric pressure and the evacuated sample environment. Fluid handling was performed using a combination of peristaltic (Perimax, SPETEC GmbH, Germany), pressure-driven (Flow EZ 2000, Fluigent, France), and syringe pumps (540060, TSE Systems GmbH, Germany), allowing flexible control of flow conditions during system preparation, sample loading, trapping, and imaging. Before the experiments, the complete fluidic path, including tubing and the microfluidic chip, was flushed using the peristaltic pump to remove air bubbles and contaminants and to ensure

 This journal is © The Royal Society of Chemistry 2026

stable laminar flow. During experiments, fluid flow was primarily controlled using the pressure-based pump coupled to an inline flow sensor, enabling continuous monitoring and regulation of the flow rate. Buffer or culture medium was initially introduced at high flow rates to rapidly fill the system and transport the sample to the observation region. The flow rate was then progressively reduced to enable DEP manipulation and positioning of individual cells within the microfluidic channel. For fine positioning near the trapping region, flow rates in the range of a few microliters per hour were employed. For high-precision flow control during the final trapping step, the syringe pump equipped with a glass micro-syringe was used to deliver microliter-scale volumes at stable low flow rates. This configuration ensured reproducible hydrodynamic conditions during activation of the DEP electrodes and trapping within the field cage. During VIS imaging, a residual low flow was maintained to limit local heating and provide continuous medium exchange. For SXR exposure, the flow was paused to ensure positional stability of the trapped sample.

Electrical interfacing and electrode control

Electrical connection to the microfluidic chip was established through a dedicated vacuum feedthrough (CF63 SUBD 25 B, VACOM GmbH, Germany), enabling signal transmission between the external electronics and the electrodes integrated on the chip. Inside the vacuum chamber, electrical contact to the chip pads was provided by spring-loaded pin contacts (Series 854, Mill-Max, USA) mounted in the MFC housing, ensuring reliable and reproducible electrical interfacing. The DEP electrodes were driven by custom multichannel signal generators delivering square-wave signals with adjustable frequency and voltage amplitude, allowing independent control of individual electrode groups. Separate generators were used to power the electrodes forming the field cage and the auxiliary electrodes employed for particle control inside the microchannel. All experiments were performed at a fixed excitation frequency of 1 MHz, while the applied voltage was varied according to the trapping conditions. Signal generation and electrode activation were controlled *via* custom software, enabling real-time adjustment of frequency, voltage and phase during experiments.

Correlative SXR and VIS microscopy setup

The microfluidic cell was tested using a custom-built correlative microscope combining SXR imaging with VIS microscopy (Reinhard *et al.*, 2023).[35] Soft X-rays were generated by a laser-produced plasma source based on a gas-puff target. Due to the strong absorption of WW radiation in air, the entire beam path, including the sample environment, was operated under high-vacuum conditions ($\approx 10^{-5}$ mbar). An ellipsoidal mirror (Rigaku) served as a condenser to collect and focus the X-ray emission onto the sample. The MFC was mounted on a motorised stage with horizontal and vertical translation. Imaging was performed using a Fresnel zone plate (Zoneplates Ltd.; 180 μm diameter, 33 nm outermost zone width) as the objective onto a CCD camera (Andor iKon-L). The system achieves a half-pitch resolution of 50 nm. A visible-light bright-field epifluorescence microscope was integrated into the SXR setup, enabling multicolor fluorescence imaging using three excitation channels (DAPI, GFP, and DeepRed). Excitation light was delivered *via* a fiber-coupled LED source. Only the objective lens (Olympus RMS10×) was located inside the vacuum chamber, while filters and detection optics were positioned externally. This configuration enabled rapid removal of fluorescence filters and thus supported bright-field imaging of the microfluidic windows, including non-fluorescent samples. The fluorescence objective and the SXR zone plate were mounted on a shared motorized stage, allowing switching between imaging modalities without repositioning the sample. The MFC was integrated into the microscope by replacing the standard sample holder and mounting it onto the existing positioning stages. For alignment, the zone plate was moved out of the beam path and the MFC was positioned to maximize and homogenize the transmitted X-ray signal on the detector.

Vacuum compatibility and pressure stability test

To verify the vacuum compatibility and operational stability of the MFC, the system was evacuated and the chamber pressure was continuously monitored, with particular attention to the pressure response during liquid introduction into the MFC. Previous tests showed that insufficient sealing leads to distinct pressure fluctuations or sudden pressure increases during liquid flow. Accordingly, the absence of pressure variations during initial fluid injection and subsequent steady flow was used as an indicator of proper sealing and stable microfluidic operation under vacuum conditions. In parallel, the microfluidic channel was inspected optically using the integrated VIS microscope to verify the absence of trapped air bubbles within the visible region of the channel.

Sample loading, dielectrophoretic trapping, and image acquisition

For image acquisition, the zone plate was aligned to the sample using a closed loop nanopositioning stage. The optimal focal plane was determined by acquiring a series of 210 s exposures while incrementally approaching the sample. Initial coarse alignment was performed by imaging the electrodes located on the upper and lower Si_3N_4 membranes, using the known membrane separation as a geometric reference to approximate the focal position midway between the membranes. Final fine focusing was verified by assessing the sharpness of structural features within the sample. Image acquisition was subsequently carried out by summing multiple individual exposures of 120–210 s each, depending on the sample (120 s for polystyrene microparticles and 210 s for living cells). For the images shown in Fig. 6c and d, the

effective integration time was limited to approximately 1–1.25 h due to cell motion. The extended integration time was attributed to the increased thickness of the liquid layer, which results from membrane deformation under differential pressure.

Before sample injection, the microfluidic system was filled with a physiologically compatible buffer or culture medium to ensure appropriate electrical conductivity for dielectrophoretic manipulation. Samples were introduced into the MFC from a sealed reservoir using the pressure-driven pump and transported to the observation region at elevated flow rates. Once particles or cells reached the imaging window, the flow rate was gradually reduced to enable DEP-based manipulation and section. For fine control during trapping, the flow was further reduced using a syringe pump. Target objects were initially pre-trapped at hook-shaped electrodes and subsequently guided into the DEP field cage, where contactless immobilization was achieved. During imaging, fluid flow was stopped to minimize hydrodynamic disturbances and maximize trapping stability. After completion of imaging, the dielectrophoretic field was switched off and the trapped object was released. The same trapping sequence was applied to both reference microparticles and biological samples.

Sample preparation and cell culture

Both polystyrene microparticles and biological samples were used in this study. Polystyrene samples consisted of fluorescent microbeads, while biological specimens included human cells, used during the development and evaluation of the field cage for trapping stability (Trapping Stability in the SI), and photosynthetic microorganisms, employed for SXR imaging. Sample preparation protocols were adapted to ensure compatibility with microfluidic handling and DEP manipulation. Polystyrene microbeads with diameters of 3.0–4.5 μm (17147–17135, Polysciences Inc., USA) were used. Stock suspensions were prepared in ultrapure water containing a non-ionic surfactant and subsequently serially diluted to obtain working concentrations of approximately 10^5 beads per mL prior to injection.

Jurkat cells (Clone E6-1, ATCC, USA) were cultured under standard conditions in supplemented RPMI medium (P04-18000, PAN-Biotech, Germany) at 37 °C and 5% CO_2. Cultures of photosynthetic microorganisms were maintained in suspension cultures with BG-11 medium at 30 °C and under continuous illumination of approximately 50 μmol photons m^{-2} s^{-1}. Cultures were periodically refreshed to maintain stable growth. Prior to soft X-ray imaging, cell suspensions were diluted to concentrations of approximately 10^5 cells per mL, suitable for microfluidic loading and dielectrophoretic trapping.

Real-time fluorescence imaging during trapping

The visible-light microscope integrated into the SXR microscopy setup enabled real-time observation of the trapping process. Cells were continuously monitored under bright-field illumination with exposure times of 5 ms until a suitable target cell was identified and successfully pre-trapped at the hook electrode. The trapped cell was subsequently guided into the field cage, where it was positioned using the integrated electrodes at a location suitable for SXR microscopy. After positioning, VIS images were acquired with exposure times ranging from 5 to 500 ms, depending on the fluorescence brightness of the sample. These images were used to confirm the presence of sufficient fluorescence signal and to verify the visibility of relevant structures for subsequent SXR imaging.

SXR exposure, image acquisition, and post-imaging analysis

After completion of fluorescence-based positioning, the microscope was switched to the SXR imaging mode. The shared motorized stage for the visible-light objective and the Fresnel zone plate ensured precise spatial overlap between the SXR images and the previously acquired VIS images, as the relative alignment of the optical components was fixed. Consequently, no additional repositioning of the sample was required when switching between imaging modalities. Focusing and SXR image acquisition were performed as described for the reference sample. Upon completion of the SXR measurements, the system was switched back to the visible-light mode to verify that the sample remained at its original position throughout the imaging sequence. In visible-light mode, the imaged cell was flushed out of the microfluidic system to allow trapping of a new target cell or complete exchange of the sample. The flushing process was monitored optically to ensure complete removal of the residual material from the microchannel.

Flushing, cleaning, and system reconditioning

After imaging, the microfluidic system was flushed to remove residual samples. Flushing was performed using ultrapure water delivered *via* the pressure-driven pump and was monitored in visible-light mode to ensure complete removal of particles or cells from the microchannel and confirm that only clear water was flowing through the device. If the residual biological material remained attached to the channel surfaces, an additional enzymatic rinse was applied to facilitate detachment, followed by thorough flushing with ultrapure water. At the end of each experimental session, the microfluidic system was flushed with ultrapure water and subsequently dried with N_2. The vacuum chamber remained sealed, and the flow cell was kept under vacuum conditions to preserve system integrity for subsequent experiments. Ultrapure water flushing was used in the present study to remove the residual material between the dilute aqueous samples investigated here. This procedure should not be interpreted as a universal method for preventing aggregation or fouling, as the appropriate cleaning strategy depends on

 This journal is © The Royal Society of Chemistry 2026

the sample and medium. The chemical compatibility of the fully assembled device with organic solvents or acidic and alkaline cleaning solutions was not systematically evaluated.

Conclusions

In this work, we presented a vacuum-compatible microfluidic flow cell for water-window soft X-ray microscopy that combines X-ray-transparent liquid confinement with integrated dielectrophoretic trapping and sample exchange. The platform enables positioning and confinement of suspended particles and cells within a thin liquid layer while maintaining compatibility with the high-vacuum environment required for SXR imaging.

The device demonstrated reliable sealing, stable operation over extended experimental periods, and fluidic sample exchange without venting the microscope vacuum. Integration of dielectrophoretic trapping with microfluidic handling enabled controlled positioning of individual specimens and facilitated consecutive measurements of different samples during a single vacuum session. The dual-pump architecture provided flexible transitions between loading, trapping, imaging, and cleaning procedures while maintaining stable operating conditions.

Combined with a laboratory-based water-window SXR microscope, the platform enabled imaging of dielectrophoretically trapped algal cells in liquid and demonstrated the feasibility of integrating DEP-based cell handling, microfluidic sample exchange, and SXR microscopy within a single experimental system.

These results establish a foundation for future studies requiring controlled manipulation and imaging of hydrated suspended cells under water-window SXR conditions and provide a versatile platform for further developments in microfluidic sample environments for soft X-ray microscopy.

Author contributions

Conceptualization: SdC, JRo, MK, NG, SF, GGP, WE, LL. Methodology: SdC, NG, MK. Investigation: SdC, JRe, SK. Fabrication: SdC, CGM, CL. Software: NG, SdC. Visualization: SdC, NG, MK. Supervision: NG, MK, GGP, SF. Writing – original draft: SdC. Writing – review & editing: SdC, NG, MK, JRe, SK, SF, JRo, WE, CL, MV, JZ, LL, GGP.

Conflicts of interest

There are no conflicts to declare.

Data availability

The data supporting this article have been included as part of the supplementary information (SI).

Supplementary information: schemes detailing the different operation modes of the dielectrophoretic field cage and images and videos of dielectrophoretically trapped and positioned cells and particles are provided and form the basis for our analyses of cage-based dielectrophoretic cell trapping, trapping stability and controlled positioning of single cells in liquid. See DOI: https://doi.org/10.1039/d6lc00276e.

Acknowledgements

This work was made possible through cross-institutional collaboration involving multiple research teams. The authors acknowledge Erik Hahn for his contribution to the MFC design and the SciTec Department of the Ernst-Abbe-Hochschule Jena for customized laser processing of silicon frames. The authors would like to thank Dr. Christina Wichmann for providing sample materials for pre-tests and for her support during this study. Marine Vallet is supported by DFG, SFB1127 ChemBioSys, project number 239748522. Max Planck Institute for Chemical Ecology is acknowledged for hosting algal culture facilities of Marine Vallet. This work was supported by the Fraunhofer Cluster of Excellence Advanced Photon Sources and by the German Research Foundation DFG under project number 405054418.

References

1 S. A. Golyshev, E. P. Kazakov, I. I. Kireev, D. G. Reunov and I. V. Malyshev, *Acta Naturae*, 2023, **15**, 32–43.
2 M. J. Moore, J. A. Sebastian and M. C. Kolios, *J. Biomed. Opt.*, 2019, **24**, 1.
3 T. C. von Erlach, S. Bertazzo, M. A. Wozniak, C.-M. Horejs, S. A. Maynard, S. Attwood, B. K. Robinson, H. Autefage, C. Kallepitis, A. del Río Hernández, C. S. Chen, S. Goldoni and M. M. Stevens, *Nat. Mater.*, 2018, **17**, 237–242.
4 M. Boutros, F. Heigwer and C. Laufer, *Cell*, 2015, **163**, 1314–1325.
5 M.-C. Hung and W. Link, *J. Cell Sci.*, 2011, **124**, 3381–3392.
6 S. J. Altschuler and L. F. Wu, *Cell*, 2010, **141**, 559–563.
7 C. A. Larabell and K. A. Nugent, *Curr. Opin. Struct. Biol.*, 2010, **20**, 623–631.
8 B. Abhisheka, S. K. Biswas, B. Purkayastha, D. Das and A. Escargueil, *Multimed. Tools Appl.*, 2023, **83**, 43035–43070.
9 S. Hussain, I. Mubeen, N. Ullah, S. S. U. D. Shah, B. A. Khan, M. Zahoor, R. Ullah, F. A. Khan and M. A. Sultan, *BioMed Res. Int.*, 2022, 5164970.
10 S. Liu, P. Hoess and J. Ries, *Annu. Rev. Biophys.*, 2022, **51**, 301–326.
11 T. Stuart and R. Satija, *Nat. Rev. Genet.*, 2019, **20**, 257–272.
12 C. Brasko, K. Smith, C. Molnar, N. Farago, L. Hegedus, A. Balind, T. Balassa, A. Szkalisity, F. Sukosd, K. Kocsis, B. Balint, L. Paavolainen, M. Z. Enyedi, I. Nagy, L. G. Puskas, L. Haracska, G. Tamas and P. Horvath, *Nat. Commun.*, 2018, **9**, 226.
13 J. C. Caicedo, S. Cooper, F. Heigwer, S. Warchal, P. Qiu, C. Molnar, A. S. Vasilevich, J. D. Barry, H. S. Bansal, O. Kraus, M. Wawer, L. Paavolainen, M. D. Herrmann, M. Rohban, J. Hung, H. Hennig, J. Concannon, I. Smith, P. A. Clemons, S. Singh, P. Rees, P. Horvath, R. G. Linington and A. E. Carpenter, *Nat. Methods*, 2017, **14**, 849–863.

14 M. J. T. Stubbington, O. Rozenblatt-Rosen, A. Regev and S. A. Teichmann, *Science*, 2017, **358**, 58–63.
15 C. Trapnell, *Genome Res.*, 2015, **25**, 1491–1498.
16 P. K. Chattopadhyay, T. M. Gierahn, M. Roederer and J. C. Love, *Nat. Immunol.*, 2014, **15**, 128–135.
17 K. Taniguchi, T. Kajiyama and H. Kambara, *Nat. Methods*, 2009, **6**, 503–506.
18 L. Schermelleh, A. Ferrand, T. Huser, C. Eggeling, M. Sauer, O. Biehlmaier and G. P. C. Drummen, *Nat. Cell Biol.*, 2019, **21**, 72–84.
19 S. W. Hell, *Nat. Methods*, 2009, **6**, 24–32.
20 M. J. Rust, M. Bates and X. Zhuang, *Nat. Methods*, 2006, **3**, 793–796.
21 E. Betzig, G. H. Patterson, R. Sougrat, O. W. Lindwasser, S. Olenych, J. S. Bonifacino, M. W. Davidson, J. Lippincott-Schwartz and H. F. Hess, *Science*, 2006, **313**, 1642–1645.
22 S. T. Hess, T. P. K. Girirajan and M. D. Mason, *Biophys. J.*, 2006, **91**, 4258–4272.
23 T. A. Klar, S. Jakobs, M. Dyba, A. Egner and S. W. Hell, *Proc. Natl. Acad. Sci. U. S. A.*, 2000, **97**, 8206–8210.
24 V. Weinhardt and C. Larabell, *Annu. Rev. Anal. Chem.*, 2025, **18**, 427–446.
25 T. H. Coale, V. Loconte, K. A. Turk-Kubo, B. Vanslembrouck, W. K. E. Mak, S. Cheung, A. Ekman, J.-H. Chen, K. Hagino, Y. Takano, T. Nishimura, M. Adachi, M. Le Gros, C. Larabell and J. P. Zehr, *Science*, 2024, **384**, 217–222.
26 M. Harkiolaki, M. C. Darrow, M. C. Spink, E. Kosior, K. Dent and E. Duke, *Emerging Top. Life Sci.*, 2018, **2**, 81–92.
27 B. Rösner, S. Finizio, F. Koch, F. Döring, V. A. Guzenko, M. Langer, E. Kirk, B. Watts, M. Meyer, J. Loroña Ornelas, A. Späth, S. Stanescu, S. Swaraj, R. Belkhou, T. Ishikawa, T. F. Keller, B. Gross, M. Poggio, R. H. Fink, J. Raabe, A. Kleibert and C. David, *Optica*, 2020, **7**, 1602.
28 D. A. Shapiro, Y.-S. Yu, T. Tyliszczak, J. Cabana, R. Celestre, W. Chao, K. Kaznatcheev, A. L. D. Kilcoyne, F. Maia, S. Marchesini, Y. S. Meng, T. Warwick, L. L. Yang and H. A. Padmore, *Nat. Photonics*, 2014, **8**, 765–769.
29 A. Sakdinawat and D. Attwood, *Nat. Photonics*, 2010, **4**, 840–848.
30 G. Schneider, P. Guttmann, S. Heim, S. Rehbein, F. Mueller, K. Nagashima, J. B. Heymann, W. G. Müller and J. G. McNally, *Nat. Methods*, 2010, **7**, 985–987.
31 G. Schneider, *Ultramicroscopy*, 1998, **75**, 85–104.
32 J. Kirz, C. Jacobsen and M. Howells, *Q. Rev. Biophys.*, 1995, **28**, 33–130.
33 H. Jiang, C. Song, C.-C. Chen, R. Xu, K. S. Raines, B. P. Fahimian, C.-H. Lu, T.-K. Lee, A. Nakashima, J. Urano, T. Ishikawa, F. Tamanoi and J. Miao, *Proc. Natl. Acad. Sci. U. S. A.*, 2010, **107**, 11234–11239.
34 J. Maser, A. Osanna, Y. Wang, C. Jacobsen, J. Kirz, J. Spector, B. Winn and D. Tennant, *J. Microsc.*, 2000, **197**, 68–79.
35 J. Reinhard, S. Kaleta, J. J. Abel, F. Wiesner, M. Wünsche, E. Seemann, M. Westermann, T. Weber, J. Nathanael, A. Iliou, H. Fiedorowicz, F. Hillmann, C. Eggeling, G. G. Paulus and S. Fuchs, *Microsc. Microanal.*, 2023, **29**, 2014–2025.
36 P. A. C. Takman, H. Stollberg, G. A. Johansson, A. Holmberg, M. Lindblom and H. M. Hertz, *J. Microsc.*, 2007, **226**, 175–181.
37 H. Stollberg, M. Pokorny and H. M. Hertz, *J. Microsc.*, 2007, **226**, 71–73.
38 B. Weinhausen and S. Köster, *Lab Chip*, 2012, **13**, 212–215.
39 X. Mei, H.-C. Lee, K. Diao, M. Huang, B. Lin, C. Liu, Z. Xie, Y. Ma, P. M. Robson, M. Chung, A. Bernheim, V. Mani, C. Calcagno, K. Li, S. Li, H. Shan, J. Lv, T. Zhao, J. Xia, Q. Long, S. Steinberger, A. Jacobi, T. Deyer, M. Luksza, F. Liu, B. P. Little, Z. A. Fayad and Y. Yang, *Nat. Med.*, 2020, **26**, 1224–1228.
40 D. P. Clark and C. T. Badea, *Phys. Med.*, 2014, **30**, 619–634.
41 Th. Schnelle, T. Müller and G. Fuhr, *J. Electrost.*, 2000, **50**, 17–29.
42 M. Kirschbaum, C. R. Guernth-Marschner, S. Cherré, A. de Pablo Peña, M. S. Jaeger, R. A. Kroczek, T. Schnelle, T. Mueller and C. Duschl, *Lab Chip*, 2012, **12**, 443.
43 M. Habaza, M. Kirschbaum, C. Guernth-Marschner, G. Dardikman, I. Barnea, R. Korenstein, C. Duschl and N. T. Shaked, *Adv. Sci.*, 2017, **4**, 1600205.
44 T. Müller, A. Pfennig, P. Klein, G. Gradl, M. Jäger and T. Schnelle, *IEEE Eng. Med. Biol. Mag.*, 2003, **22**, 51–61.
45 T. Gerling, N. Godino, F. Pfisterer, N. Hupf and M. Kirschbaum, *Lab Chip*, 2023, **23**, 3172–3185.
46 F. Pfisterer, N. Godino, T. Gerling and M. Kirschbaum, *RSC Adv.*, 2023, **13**, 19379–19387.
47 N. Godino, F. Pfisterer, T. Gerling, C. Guernth-Marschner, C. Duschl and M. Kirschbaum, *Lab Chip*, 2019, **19**, 4016–4020.
48 M. Kirschbaum, M. S. Jaeger and C. Duschl, *Lab Chip*, 2009, **9**, 3517.
49 M. Kirschbaum, M. S. Jaeger, T. Schenkel, T. Breinig, A. Meyerhans and C. Duschl, *J. Chromatogr. A*, 2008, **1202**, 83–89.
50 C. Duschl, P. Geggier, M. Jäger, M. Stelzle, T. Müller, T. Schnelle and G. R. Fuhr, in *Lab-on-Chips for Cellomics*, ed. H. Andersson and A. van den Berg, Springer Netherlands, Dordrecht, 2004, pp. 83–122.
51 A. Ramos, H. Morgan, N. G. Green and A. Castellanos, *J. Phys. D: Appl. Phys.*, 1998, **31**, 2338–2353.
52 R. Pethig, *Biomicrofluidics*, 2010, **4**, 022811.
53 T. Schnelle, R. Hagedorn, G. Fuhr, S. Fiedler and T. Müller, *Biochim. Biophys. Acta, Gen. Subj.*, 1993, **1157**, 127–140.
54 T. Zavřel, P. Očenášová and J. Červený, *PLoS One*, 2017, **12**, e0189130.
55 R. Wang, Q. Zhao, L. Loetgering, F. Allars, Z. Hong, T. J. Pennycook, R. Horstmeyer, J. Rodenburg, A. Maiden and G. Zheng, *Nat. Rev. Methods Primers*, 2025, **5**, 68.
56 C. Liu, L. Licht and J. Rothhardt, *Ultramicroscopy*, 2026, **283**, 114337.
57 M. W. M. Jones, K. D. Elgass, M. D. Junker, M. D. de Jonge and G. A. van Riessen, *Sci. Rep.*, 2016, **6**, 24280.

This journal is © The Royal Society of Chemistry 2026